JACS Au
AN OPEN ACCESS JOURNAL OF THE AMERICAN CHEMICAL SOCIETY

pubs.acs.org/jacsau
Letter

The Identity of Nickel Peroxide as a Nickel Superoxyhydroxide for Enhanced Electrocatalysis

Yizhou Yang,[▽] Jili Li,[▽] Chong Li, Ming Gong,* Xue Wang, Xuejing Yang,* Hualin Wang, Ye-Fei Li,* and Zhi-Pan Liu

Cite This: *JACS Au* 2023, 3, 2964−2972

Read Online

ACCESS | Metrics & More | Article Recommendations | Supporting Information

ABSTRACT: Nickel peroxides are a class of stoichiometric oxidants that can selectively oxidize various organic compounds, but their molecular level structure remained elusive until now. Herein, we utilized structural prediction using the Stochastic Surface Walking method based on a neural network potential energy surface and advanced characterization using the as-synthesized nickel peroxide to unravel its chemical identity as the bridging superoxide containing nickel hydroxide, or nickel superoxyhydroxide. Superoxide incorporation tunes the local chemical environment of nickel and oxygen beyond the conventional Bode plot, offering a 6.4-fold increase in the electrocatalytic activity of urea oxidation. A volcanic dependence of the activity on the oxygen equivalents leads to the proposed active site of the Ni(OO)(OH)Ni five-membered ring. This work not only unveils the possible structures of nickel peroxides but also emphasizes the significance of tailoring the oxygen environment for advanced catalysis.

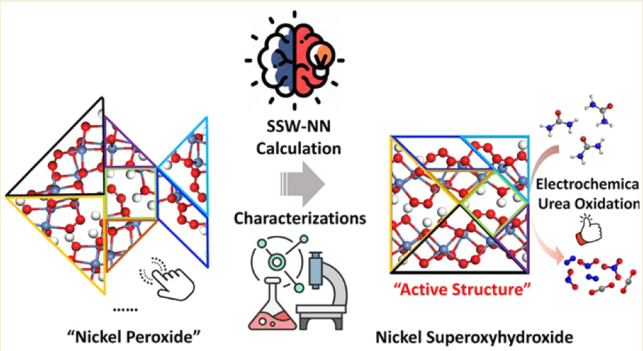

KEYWORDS: *Nickel peroxide, Structure prediction, Superoxide, Oxygen species, Electrochemistry*

Nickel peroxide, a term coined in the last century by organic chemists, refers to a class of stoichiometric oxidants that can efficiently oxidize various organic compounds.[1] It was often synthesized by the chemical oxidation of nickel hydroxide ($Ni(OH)_2$) using strong oxidants, such as ozone (O_3), sodium hypochlorite (NaClO), and sodium/potassium persulfate ($Na_2S_2O_8/K_2S_2O_8$).[2−4] These oxidants have very high oxidative power and can be subject to various chemical transformations (e.g., oxygen atom transfer, hydrogen abstraction, secondary radical formation, etc.),[5−9] which can result in strong uncertainties on the nickel peroxide structures. One structural analog is nickel oxyhydroxide (NiOOH) with partially dehydrogenated $Ni(OH)_2$, often proposed as the active phase for the electrocatalytic selective oxidation reaction (SOR) and oxygen evolution reaction (OER).[10−14] However, some fragmentary evidence by X-ray photoelectron spectroscopy (XPS) and thermogravimetric analysis (TGA) has revealed slight differences between nickel peroxide and NiOOH,[15−18] but the detailed molecular-level structure and the origin of its oxidation activity is still under debate. Recognizing its structure could not only resolve a long-lasting mystery but also potentially extend beyond the Bode plot to tune the local Ni coordination environment for the development of next-generation Ni-based electrocatalysts.[19−21]

Structural prediction via theoretical calculation has emerged as a powerful tool for chemists owing to the rapidly developing computing power.[22−25] At least thousands of minima are generally required to determine the structure from a single composition to ensure the reliability; however, that is expensive for first-principles calculations.[26−28] Recently, a neural network (NN) potential energy surface (PES) has been demonstrated to speed up the calculations while maintaining first-principles accuracy.[29,30] The key challenge of fitting the NN PES is generating a good data set, which in most cases is obtained from trajectories of molecular dynamics (MD) simulations that cannot describe chemical reactions. Accordingly, the Stochastic Surface Walking (SSW) global optimization tool[31−33] was proposed by our group for generating a database via a smooth trajectory.[34,35] The SSW method is an approach that lies between molecular dynamics (MD) and basin hoping[36−38] and genetic algorithm,[39,40] which can effectively overcome energy barriers and meanwhile retains information about the evolution of atomic motion.[41−43] As a result, structures generated by the SSW method are evenly

Received: May 15, 2023
Revised: October 18, 2023
Accepted: October 20, 2023
Published: November 2, 2023

https://doi.org/10.1021/jacsau.3c00245
JACS Au 2023, 3, 2964−2972

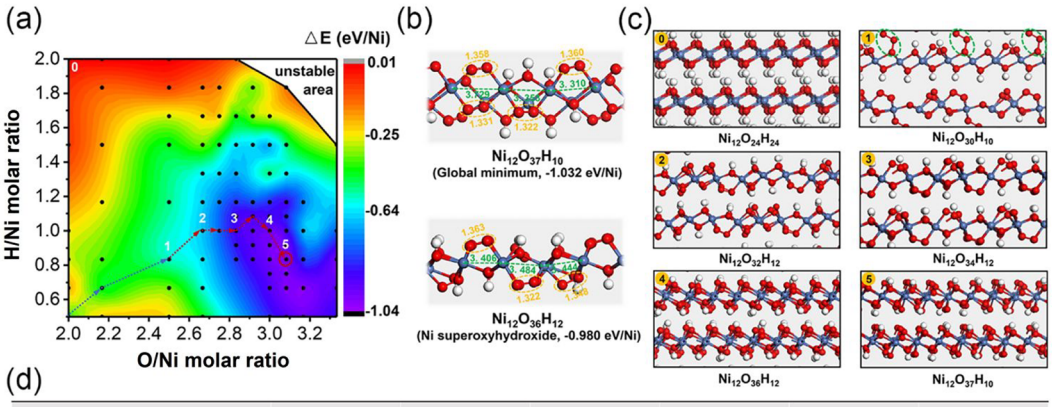

(d)

		$Ni_{12}O_{24}H_{24}$	$Ni_{12}O_{30}H_{10}$	$Ni_{12}O_{32}H_{12}$	$Ni_{12}O_{34}H_{12}$	$Ni_{12}O_{36}H_{12}$	$Ni_{12}O_{37}H_{10}$
Unit cell size	*a* (Å)	7.22	8.48	9.68	9.14	10.24	8.84
	b (Å)	10.90	6.06	10.46	9.00	8.96	8.68
	c (Å)	6.31	10.26	6.32	6.92	6.80	8.28
	α (°)	89.99	99.99	94.00	95.75	89.29	74.44
	β (°)	90.00	98.96	108.20	83.49	108.04	93.10
	γ (°)	100.79	80.16	64.62	99.49	94.29	88.09
Oxygen species number	^{b}O	0	6	4	2	0	1
	^{b}OO	0	4	8	10	12	13
	^{b}OH	24	10	12	12	12	10
	$^{i}O_3$	0	2	0	0	0	0

Figure 1. (a) Contour plot of the grand potential surface of nickel peroxide using O_3 as an oxidant, where the black dots represent the calculated stoichiometries and the arrows index the structural evolution with the lowest energy point of each O/Ni ratio. (b) Two typical structures of nickel peroxides with the lowest energies. (c) Several structures of the representative compositions indexed in panel a, and (d) the corresponding summary table of unit cell parameters and oxygen species. The green circle highlights the ozone fragment. The blue balls are Ni; red balls are O; white balls are H.

distributed on the PES and cover a wide region of the PES (see SI for more details).

Herein, we first adopted a global structural search based on SSW-NN PES[34,44] to glean the possible nickel peroxide structures via simple Ni/O/H stoichiometries (Figures 1 and S3−S5). Since the nickel peroxide is made using O_3 as an oxidant (a standard method to achieve nickel peroxides in previous literature[45,46]), we used eq 1 to estimate the formation free energy of nickel peroxides with dissimilar chemical components. We constructed a series of $Ni_{12}O_{24+x}H_{24-y}$ unit cells ($0 \le x \le 16$ and $0 \le y \le 18$), and compared their structural viability. For each stoichiometry, we examined at least 10^4 local minima via SSW-NN and then confirmed the results by density functional theory (DFT). The exchange-correlation energy is treated on the generalized gradient approximation (GGA) by using the Hubbard term corrected DFT functional, PBE + U.[47] The effective value for Hubbard terms (U_{eff}) is set as 5.5 eV for Ni.[48]

$$Ni(OH)_2 + xO_{3(g)} \rightarrow NiO_{2+x}H_{2-y} + (x - \frac{y}{4})O_{2(g)} + \frac{y}{2}H_2O_{(g)} \quad (1)$$

The grand potential surface shows lower energies at larger oxygen stoichiometries (Figure 1a), indicating a high level of oxygen incorporation in nickel peroxide. The global minimum (GM, No. 5) is located around $Ni_{12}O_{37}H_{10}$ with a free energy change of −1.03 eV/Ni, which is more stable than $Ni_{12}O_{24}H_{12}$ (NiOOH) by −0.75 eV/Ni. Note that the higher stability of $Ni_{12}O_{37}H_{10}$ compared to NiOOH is because a relatively high oxygen chemical potential ($\mu_O = G[O_3] - G[O_2]$) is used in calculations, which represents a strong oxidation environment in the experiments.

In the GM structure, we observed a large content of bridging O−O dimers (abbreviated as ^{b}OO, 13 ^{b}OO units for 12 Ni) (Figure 1b). The desorption free energy changes of these O−O dimers are positive (e.g., +0.83 eV, where the free energy of reference O_2 molecule is calculated by $G[O_2] = 2G[H_2O] - 2G[H_2]$ to avoid the overbinding error of O_2 calculated in DFT), confirming the high stability of the O−O dimer. The ^{b}OO dimers have O−O distances of 1.322−1.360 Å and on-site spins of 0.46−0.74 μ_B, both representing a chemical nature between superoxides and peroxides (closer to superoxides). The Ni−Ni distances buckled by ^{b}OO dimers (3.310−3.729 Å) are significantly longer compared to the 3.156 and 2.782−3.094 Å in $Ni(OH)_2$ and NiOOH, respectively (The divergent Ni−O bond lengths in NiOOH are caused by the Jahn−Teller effect of Ni^{3+}). It is worth noting that the extra oxygen incorporation does not raise the Ni valence much (average +2.49 for $Ni_{12}O_{37}H_{10}$) but exerts its oxidative power to the O valence (average −1.41 for ^{b}OO in $Ni_{12}O_{37}H_{10}$), which probably explains its activity origin as the stoichiometric oxidant.

Since dehydrogenation is relatively easier than oxygenation, we find the structures with the lowest energies for each O/Ni ratio to delineate a structural-evolution path under synthetic conditions (Figure 1a). Under the ratio of 2/1, the most stable structure resides at a low hydrogen stoichiometry, implying thermodynamically favorable $Ni(OH)_2$ oxidation in O_3. The gradual oxygen incorporation follows a horizontal path with only slight fluctuations of the hydrogen stoichiometries, suggesting that the superoxides are replacing the oxides rather than the hydroxides. Indeed, the local minima of $Ni_{12}O_{30}H_{10}$ exhibit the displacement of bridging oxides (^{b}O) by ozone fragments ($^{i}O_3$) while maintaining the hydroxide components (^{b}OH) (No. 1 in Figure 1c). These ozone fragments can be

https://doi.org/10.1021/jacsau.3c00245
JACS Au 2023, 3, 2964−2972

gradually converted to ^{b}OO units upon increasing oxygen stoichiometries. Further increasing oxygen stoichiometries beyond the GM could distort the Ni−O layers, consequently decreasing its stability.

Note that a stoichiometric structure of NiOOOH ($Ni_{12}O_{36}H_{12}$, nickel superoxyhydroxide) could be obtained along the structural-evolution path, with only 0.052 eV/Ni higher than the GM. This structure is highly symmetrical with half ^{b}OO and half ^{b}OH distributed along the Ni centers. Under the grand potential surface with reference to O_2/H_2O instead of O_3, the NiOOOH is more stable than the GM (Figure S3), indicating that it could be a possible intrinsic structure of nickel peroxide when exposed to ambient conditions (Figure 1b). Both NiOOOH and the GM revealed the identity of superoxide-incorporating $Ni(OH)_2$ as a possible structure of nickel peroxide. To further confirm the stability of the GM structure, we performed a 10 ns NPT MD simulation for a (2 × 2 × 2) supercell for $Ni_{12}O_{37}H_{10}$ (the GM structure) using a G-NN potential. The MD trajectory shows that the nickel peroxide structure is stable without significant structural changes (see Figure S4 for details).

It should be emphasized that NiOOOH is more stable than NiOOH only when exposed to a strong oxidative agent, O_3. While in electrochemical conditions, the conventional NiOOH, in turn, becomes more stable than NiOOOH (Figure S3). But the phase diagram results cannot rule out the possibility of the presence of nickel peroxide due to the possible kinetic issues (the phase diagram only reflects the thermodynamics). In fact, the positive free energy change (∼+0.83 eV) by removing one O−O dimer from the bulk NiOOOH suggests that the kinetics may prevent NiOOOH from transforming back to NiOOH. Indeed, the experimental observations also show that the properties of the NiOOOH sample did not recover even after the removal of the O_3 conditions. For example, we observed the presence of superoxide before and after electrocatalysis, which will be discussed later.

To validate the optimized structure via SSW-NN, we experimentally characterized nickel peroxide materials. An O_3-based strategy with ultraviolet irradiation enhancement was adopted for the standard synthesis. The material (namely, NP-UV/O_3) immediately turned from green to dark with a negative shift of the valence band position, corresponding to the $Ni(OH)_2$ oxidation (Figure S5g,h). The elemental analysis revealed the stoichiometries of $Ni(OH)_2$ and NP-UV/O_3 as $NiO_{2.14}H_{2.28}$ and $NiO_{2.65}H_{2.15}$, respectively(Figure 2a). Since H_2O is inevitably introduced during the material synthesis contributing to the extra O and H stoichiometry, we further estimated the water content by the first weight loss plateau, corresponding to 3.11% and 4.53% for $Ni(OH)_2$ and NP-UV/O_3 respectively (Figure S6a). The extra H_2O content in the NP-UV/O_3 likely resulted from the generation of H_2O by reacting O_3 with $Ni(OH)_2$. After deducting the H_2O contribution to the stoichiometry, we obtained the stoichiometries of $NiO_{1.98}H_{1.96}\cdot 0.16H_2O$ and $NiO_{2.37}H_{1.63}\cdot 0.26H_2O$ for $Ni(OH)_2$ and NP-UV/O_3 respectively. $Ni(OH)_2$ possesses a highly consistent stoichiometric ratio, validating our analysis approach. The larger oxygen stoichiometry of $NiO_{2.37}H_{1.63}$ confirmed the extra oxygen incorporation from our structural prediction. The discrepancy between $NiO_{2.37}H_{1.63}$ and theoretically predicted stoichiometries could be contributed from the incomplete conversion of $Ni(OH)_2$ (Figures S5a−f and S6b). We also attempted to utilize thinner electro-

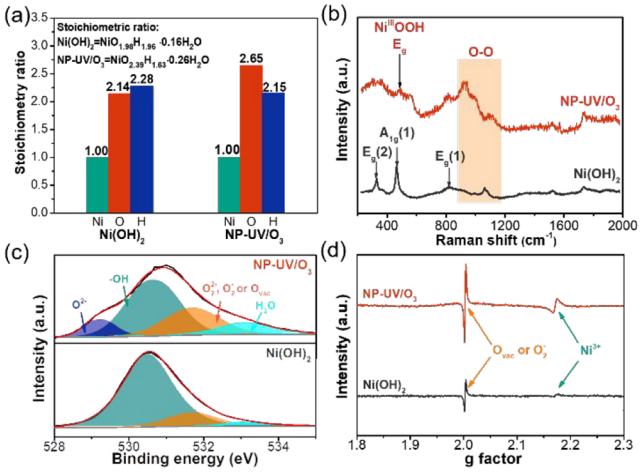

Figure 2. (a) Elemental analysis, (b) Raman spectra, (c) high resolution XPS of O 1s orbital, and (d) low temperature EPR spectra of the pristine $Ni(OH)_2$ and NP-UV/O_3 materials.

deposited $Ni(OH)_2$ precursor materials to increase the relative ratio of the nickel peroxide phase, and the XRD pattern of the derived nickel peroxide shows an additional peak at ∼16.0° with larger interlayer spacings, which agrees with our simulated XRD pattern of the GM structure (Figure S7). This corroborates the generation of the superoxyhydroxide phase during the UV/O_3 treatment. The presence of the $Ni(OH)_2$ phase still suggests that complete conversion to the pure phase is still a grand challenge. However, the extra oxygen stoichiometry in $NiO_{2.37}H_{1.63}$ coincides with the missing hydrogen stoichiometry, which correlates well with the calculated minima structures ($Ni_{12}O_{36}H_{12}$ or $Ni_{12}O_{37}H_{10}$). Considering the incomplete $Ni(OH)_2$ conversion, we could dissect the $NiO_{2.37}H_{1.63}$ into $Ni(OH)_2$ (∼63%) and nickel superoxyhydroxide ($Ni_{12}O_{36}H_{12}$ or $Ni_{12}O_{37}H_{10}$, ∼37%).

We further carried out spectroscopic analysis to glean the oxygen properties. Raman spectroscopy is a powerful tool for investigating dioxygen species owing to the unique O−O mode (Figure 2b). The $Ni(OH)_2$ peaks at 328, 462, and 818 cm^{-1} gradually disappeared upon O_3−UV treatment,[49] accompanied by the evolution of the E_g bending mode of $Ni^{III}OOH$ at 498 cm^{-1}.[50] Further prolonging the treatment generated several peaks at 926, 1000, and 1100 cm^{-1}, generally attributed to the O−O bands from the peroxide or the superoxide moieties (Figure S8). The deconvoluted O 1s XPS (Figure 2c) spectra exhibited remarkable enhancement in the peak located at 531.8 eV, corresponding to the high-valent oxygen species, such as peroxide/superoxide[51−54] and O vacancies.[55] The content of these high-valent oxygen species could reach a high level of ∼28.6% based on the deconvolution result. Meanwhile, the O^{2-} and H_2O content were also raised due to the inevitable oxidation of hydroxyls into bridging O for high-O/low-H phases (e.g., $Ni_{12}O_{37}H_{10}$) and the generated H_2O by reacting O_3 with $Ni(OH)_2$. Although we resolved the high-valent O species in Raman and XPS, it is rather difficult to differentiate the peroxide and superoxide in these broad peaks, and therefore, we further carried out low temperature EPR measurement (Figure 2d). Two resonance signals centered at g factors of 2.003 and 2.172, often designated as oxygen vacancies and Ni^{3+}, were clearly resolved.[56,57] The presence of the two peaks in $Ni(OH)_2$ originated from the incorporation of oxygen vacancies and facile oxidation of the under-

https://doi.org/10.1021/jacsau.3c00245
JACS Au 2023, 3, 2964−2972

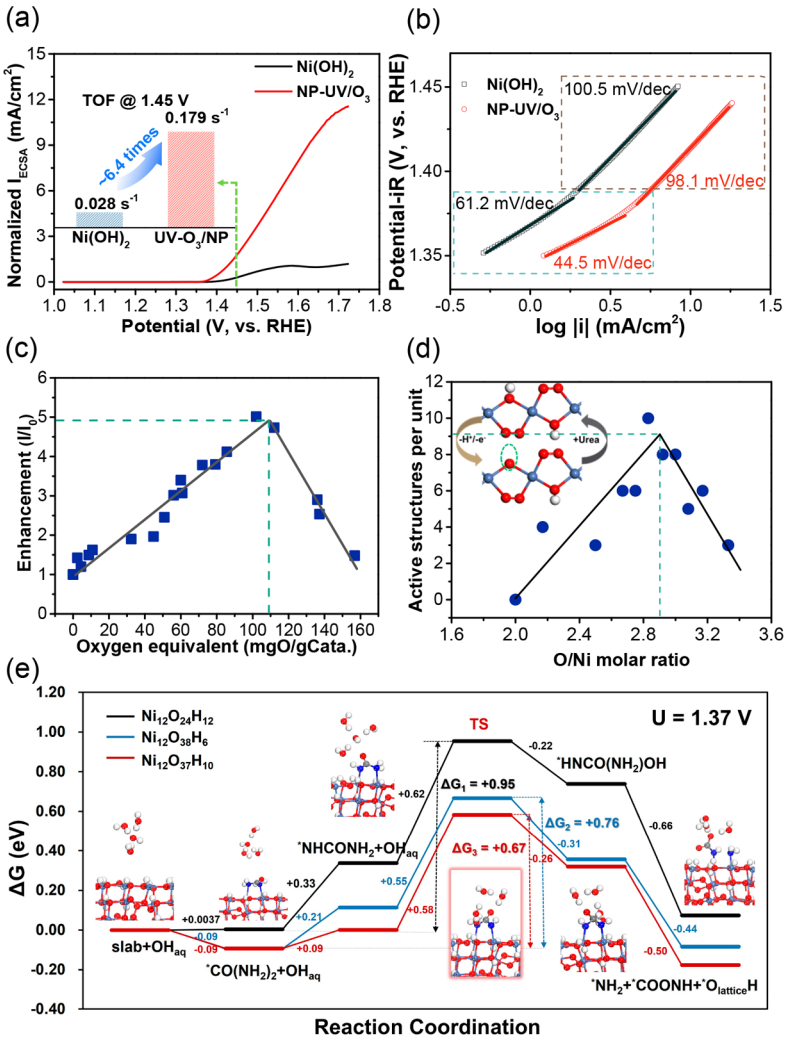

Figure 3. (a) CV curves, (b) Tafel plots, and (c) correlation between oxygen equivalent and UOR peak current enhancement factor. (d) Active structure per cell unit under different O/Ni molar ratios. Inset: schematic illustration of the bridging hydroxide/oxide cycle as the active UOR site. (e) Gibbs free energy profile for the OH^--assisted C−N cleavage pathway at 1.37 V vs RHE. The numbers between two adjacent states in the profiles represent the free energy change (in eV) of each elemental step. The structures in the figure are the atomic structures corresponding to each state of $Ni_{12}O_{37}H_{10}(10\bar{1}0)$. Colors in the Figure: Cyan balls are Ni; red balls are O; blue balls are N; gray balls are C; and white balls are H.

coordinated Ni^{2+} sites during the material synthesis. These two peaks are almost inevitable for $Ni(OH)_2$-based materials. For the NP-UV/O_3 material, it exhibited a drastic enhancement of the intensities for the two peaks. It is worthwhile to recall that the oxygen stoichiometry is higher than the value of 2 as in $Ni(OH)_2$ and NiOOH, indicating that the oxygen vacancy is not likely contributing to the enhanced signal. We note that the superoxide resonance signal also coincides with the oxygen vacancy band at g factor = 2.003,[57,58] while peroxide gives no signal at this position. Therefore, this band could be an indicator of superoxide incorporation in the material. This manifests a large extent of superoxide moieties in the nickel peroxide (Figure 2d) and supports our structural prediction.

Despite the fact that nickel peroxide is often used as a stoichiometric oxidant, regulating the Ni−O coordination by superoxide incorporation could potentially tune the local electronic states. Herein, the urea oxidation reaction (UOR) was utilized as a probe catalytic reaction, which is sensitive to its surface oxophilic structure. Cyclic voltammetry (CV) curves of $Ni(OH)_2$ and NP-UV/O_3 both exhibited characteristic UOR currents, but NP-UV/O_3 demonstrated 4.93 times higher maximal current and more negative UOR onset potentials by 49 mV (Figure S9). The electrochemical surface areas (ECSAs) were 9.68 cm^2 and 5.03 cm^2 for $Ni(OH)_2$ and NP-UV/O_3 (Figure S10), respectively, showing even lower surface areas for NP-UV/O_3. The lower ECSA after UV/O_3 treatment might be caused by the conversion of a layered $Ni(OH)_2$ phase with well-defined interlayer spacings into a relatively crowded phase with many ^{b}OO moieties. The ECSA generally scales with the treatment time with lower values under longer treatment, but when the treatment duration was more than 10 min, the ECSA started to level off, possibly due to the complete surface conversion of $Ni(OH)_2$ (Figure S10). Based on the ECSA, the calculated turnover frequency (TOF) of NP-UV/O_3 at 1.45 V vs RHE (0.179 s^{-1}) was ~6.4 times higher than that of pristine $Ni(OH)_2$ (0.028 s^{-1}), demonstrating the significantly enhanced intrinsic activity (Figure 3a).

Further Tafel kinetics study revealed two Tafel regions for UOR, and the NP-UV/O_3 only exhibited a lower Tafel slope of ~44.5 mV/decade at smaller overpotentials (compared to 61.2

https://doi.org/10.1021/jacsau.3c00245
JACS Au 2023, 3, 2964−2972

mV/decade for $Ni(OH)_2$) (Figure 3b). A Tafel slope close to 40 mV/decade indicates a rate-determining step (rds) of the second electron transfer, while the value of 60 mV/decade for $Ni(OH)_2$ corresponds to the prior step as the rds. It demonstrates that the altered energy profile upon superoxide incorporation possibly delays the rds via the facilitated electron transfer. During electrolysis, the current density at 1.623 V vs RHE showed only a slight decrease of ∼12.6% over 5 h (Figure S11a). The linear sweep voltammetry (LSV) curves after the electrolysis also confirmed good retention of the electrocatalytic performance (Figure S11b). Structural changes and amorphization are often inevitable during electrocatalysis,[59,60] so we further probed the structural stability during the UOR process. First, the macroscopic morphologies and lattice fringes were mostly maintained after electrolysis (Figures S12 and S13). The EPR spectra of the electrode before and after electrolysis showed almost identical patterns, implying the maintained superoxide moieties during UOR (Figure S14). We further investigated the evolution of superoxide species during electrocatalysis by in situ Raman spectroscopy. Upon immersing the NP-UV/O_3 material in the alkaline urea electrolyte, the characteristic OO peaks evolved at ∼1150 cm^{-1}, likely corresponding to the superoxide (Figure S15). Applying anodic potentials below 1.50 V vs RHE showed intact peaks at this position, while extending beyond 1.50 V could gradually diminish the peak due to the loss of superoxide. A similar trend was observed for consecutive scans of the Raman spectra under electrolysis at 1.45 V vs RHE and 1.55 V vs RHE. This likely indicates that the superoxide species is relatively stable under UOR conditions but not under OER conditions. Raman spectra collected in the electrolyte without urea also exhibited much higher Ni^{III}−O signals at 475 and 550 cm^{-1} with the loss of superoxide signals (Figure S16), confirming the stability hypothesis. Another structural change appeared at the O^{2-} moieties in the XPS. These O^{2-} moieties disappeared after electrolysis with the −OH percentage increased. The O^{2-} in the as-synthesized material could result from the overoxidized phases with bridging oxygen identities and higher oxygen stoichiometries, and these species could undergo the O^{2-}/−OH conversion during the electrocatalytic UOR process (Figure S17).

Another serendipitous discovery was the volcanic dependence of the UOR activity on oxygen equivalents. The effective oxygen equivalent was estimated using an iodometric method.[15,61] An optimal activity was only observed under a moderate oxygen equivalent of 109.4 mg_O/g_{Cat} (Figure 3c). According to the predicted structures of nickel peroxide, we discovered that the number of structural units of the five-membered Ni(OO)(OH)Ni ring also obeys a volcanic dependence on the oxygen equivalents (Figure 3d). We selected the representative samples with different oxygen equivalents and measured the electrochemical impedance spectroscopy to investigate the effect of ^{b}OO units or the five-membered ring unit (Figure S18). The result showed a gradual decrease of the charge transfer resistance with the initial incorporation of the ^{b}OO moieties, while the overtreatment by ozone with excessive incorporation of ^{b}OO units eventually increased the charge transfer resistance. This indicates that the introduction of ^{b}OO units to create the five-membered ring unit accelerates the interfacial electron transfer, but the overincorporation of ^{b}OO units could destruct the five-membered ring, which has a negative effect on the electron transfer capability. To further elucidate the correlation of activity, we calculated the mechanism of urea oxidation on three selected nickel peroxide surfaces with dissimilar stoichiometric ratios, $Ni_{12}O_{24}H_{12}(10\bar{1}1)$, $Ni_{12}O_{37}H_{10}(10\bar{1}0)$, and $Ni_{12}O_{38}H_6(01\bar{1}0)$, which correspond to the reference NiOOH, the global minimum (GM) of nickel peroxide, and a nickel peroxide with an even higher O/Ni ratio. We replace all the exposed surface O−O dimers by O or OH (since the removal of the exposed O−O dimer on the NiOOOH surface is exothermic), while the other O−O dimers are intact. For each surface, we considered both OH^--assisted C−N cleavage and N−N coupling mechanisms,[62] where the OH^--assisted C−N cleavage mechanism follows the * + $CO(NH_2)_2$ + OH_{aq} → *$CO(NH_2)_2$ + OH_{aq} → *$NHCONH_2$ + OH_{aq} → *$HNCO(NH_2)OH$ → *NH_2 + *COONH + *$O_{lattice}H$ pathway while the N−N coupling mechanism follows the * + $CO(NH_2)_2$ → *$CO(NH_2)_2$ → *$NHCONH_2$ → *NHCONH → *NCONH → *NNH−CO pathway. The free energy profiles of two pathways at 1.37 V vs RHE (electrode potential used in the experiment) are shown in Figure S19 and Figure S20. The results show that the OH^--assisted C−N cleavage pathway is always more favorable than the N−N coupling pathway on all three surfaces, evident from the overall free energy barrier for each pathway (see the free energy difference between TS and *$CO(NH_2)_2$ state). On the other hand, the overall free energy barriers for the OH^--assisted C−N cleavage pathway are 0.953, 0.675, and 0.761 eV for $Ni_{12}O_{24}H_{12}(10\bar{1}1)$, $Ni_{12}O_{37}H_{10}(10\bar{1}0)$, and $Ni_{12}O_{38}H_6(01\bar{1}0)$, indicating the activity of urea oxidation follows the orders of $Ni_{12}O_{37}H_{10}(10\bar{1}0)$ (O/Ni = 3.08) > $Ni_{12}O_{38}H_6(01\bar{1}0)$ (O/Ni = 3.17) > $Ni_{12}O_{24}H_{12}(10\bar{1}1)$ (O/Ni = 2.00), which is consistent with the volcanic profile observed in the experiment.

Bader charge analyses of the *$NHCONH_2$ + OH_{aq} state and the subsequent TS (see Figure 3e) were carried out to understand the origin of the enhanced UOR activity on $Ni_{12}O_{37}H_{10}$ compared to $Ni_{12}O_{24}H_{12}$. On the $Ni_{12}O_{24}H_{12}$ surface, the total Bader charges of the *$NHCONH_2$ and hydrated hydroxyl are −0.91e and −0.59e for *$NHCONH_2$ + OH_{aq} state and TS, respectively. On the $Ni_{12}O_{37}H_{10}$ surface, the total Bader charges of the same atoms are −1.07e and −0.26e for the *$NHCONH_2$ + OH_{aq} state and TS, respectively (Figure S21). Both results show that the *$NHCONH_2$ + OH_{aq} moiety tends to transfer electrons to the NiOOH/NiOOOH surfaces at the TS. Notably, the $Ni_{12}O_{37}H_{10}$ surface, with its higher oxidation state compared to $Ni_{12}O_{24}H_{12}$, facilitates this electron transfer, effectively reducing the kinetic barrier of the rate-determining step.

In summary, we adopted the SSW-NN method to rapidly determine the chemical identity of nickel peroxide as superoxide-incorporating $Ni(OH)_2$. This finding agrees well with the experimental characterizations via stoichiometric analysis showing extra oxygen and spectroscopic evidence showing O−O characteristics and superoxide spins. The nickel peroxide material could act as an efficient UOR electrocatalyst with 6.4 times higher activities. The enhanced activity was attributed to the preferred oxidation of ^{b}OH in the five-membered ring Ni(OO)(OH)Ni unit. This work not only enriches our understanding about the mystery of nickel peroxide but also creates a new route of extending beyond the Bode plot for tuning catalytic properties via a combined effort of calculation and experiment.

https://doi.org/10.1021/jacsau.3c00245
JACS Au 2023, 3, 2964−2972

MATERIALS AND METHODS

Materials and Reagents

All chemicals with analytical grade were purchased from Aladdin Bio-Chem Technology Co., LTD, Shanghai, and directly used without further purification. Carbon paper (thickness = 0.30 mm) was purchased from Hesen Electric Co., Ltd., Shanghai. Deionized water (D.I. water) used in this study was generated from a Water Purification System (>18.2 MΩ·cm^{-1}, Hitech Instruments Co., Ltd.).

Nickel Peroxide Preparation

Nickel peroxide was obtained through ozone or ozone−UV treatment of $Ni(OH)_2$ powder. $Ni(OH)_2$ powder was first synthesized by mixing nickel salt precursor and potassium hydroxide (KOH) solution: 2.907 g of $Ni(NO_3)_2{\cdot}6H_2O$ was dissolved in 100 mL of D.I. water under violent stirring for 10 min. Then, 100 mL of 200 mM KOH solution was gradually added into the Ni^{2+} solution, and the resulting suspension was ultrasonicated for 30 min. The green suspension was transferred into an 80 °C oven for 6 h to perform the aging process. Finally, the prepared $Ni(OH)_2$ was separated by filtration with alternating D.I. water and ethanol washing to remove unreacted ions, and the product powder was dried at 70 °C overnight.

The transformation of $Ni(OH)_2$ into nickel peroxide was achieved in an ozone flow atmosphere. $Ni(OH)_2$ (0.20 g) was put into a homemade glass container under continuous stirring to ensure full contact between $Ni(OH)_2$ powder and the O_3 flow. A stable flow of 1.25 mL/min was provided by a commercial ozone generator (Qingdao Guolin Environmental Technology Co., Ltd.) and injected into the glass container under ultraviolet light (Shanghai Jiguang Special Light Factory, wavelength = 253.7 nm, ∼70 W) to convert $Ni(OH)_2$ into nickel peroxide. The treatment time was adjusted to obtain nickel peroxides with different degrees of surface oxygen modification. Preparation of the thinner $Ni(OH)_2$ precursor powder was conducted by an electrodeposition method. A 0.2 M $NaNO_3$ solution was prepared by adding $NaNO_3$ powder into a 1:1 mixed solution of water and ethanol. Then, by electrodeposition under −2 V applied potential on a monolithic pure nickel electrode, the $Ni(OH)_2$ deposits on the electrode surface. The nickel electrode is subsequently moved from the electrolyte to the 1:1 mixed solution of water and ethanol and then ultrasonicated to peel off the $Ni(OH)_2$ material. After filtration, cleaning, and drying, we obtained the electrodeposited $Ni(OH)_2$ powder.

Characterizations and Analysis

X-ray diffraction (XRD) patterns were collected on a D8 Advance polycrystalline diffractometer (Bruker AXS, Co. Ltd., German) with a scan rate of 5°/min in the 2θ range from 10° to 90° (Cu Kα radiation, λ = 0.15418 nm). X-ray photoelectron spectroscopy (XPS) was carried out on a Thermo Scientific K-Alpha+ with an X-ray source of Al Kα to compare the elemental compositions and chemical states of the prepared samples, and the spectra were calibrated by C 1s binding energy of 284.6 eV. Raman spectra of the solid samples were collected on a DXR-Raman Microscope (Thermo Scientific, US) with a 532 nm laser. The in situ Raman spectra were recorded by a Raman spectrometer (Horiba Jobin Yvon) equipped with a 532 nm laser. A 2400/mm grating was used; the acquisition time was set as 30 s; the spectral Raman shift range was set from 200 to 1800 cm^{-1}. The NP-UV/O_3 catalyst for the in situ Raman spectroscopic study was prepared with catalyst loading of 0.2 mg/cm^2 on the roughened gold working electrode. The in situ Raman spectroscopy was conducted on a custom-built three-electrode cell (EC-RAIR, Beijing Science Star technology Co., Ltd.), with a Pt wire as the counter electrode and a Ag/AgCl electrode as the reference electrode (immersed in saturated KCl). The Raman spectra were collected under controlled potential electrolysis under different electrolytes, and consecutive scans were collected with a time resolution of 30 s. Elemental analysis was conducted on a LECO ONH836 analyzer (LECO, US). Nickel element content was analyzed by an inductively coupled plasma (ICP) atomic emission spectrometer (Agilent 725, US). Thermogravimetric analysis under a nitrogen atmosphere was performed on a METTLER TGA/SDTA 851e analyzer (METTLER TOLEDO, Switzerland). Paramagnetic signal of the obtained samples was recorded on an electrospin resonance spectrometer (Bruker A300, US) at 77 K by injecting liquid nitrogen. The morphology of the materials was characterized by transmission electron microscopy (TEM) (FEI Tecnai F20, US).

Electrochemical Measurement

The electrochemical measurement was conducted on an H-type electrolysis cell using Ag/AgCl and graphite rods as the reference and counter electrode, respectively. The measurement was also conducted using a Hg/HgO (1 M KOH) reference electrode to ensure the accuracy of the measured potential. One M KOH + 0.33 M urea was employed as the electrolyte, unless specified. An anion exchange membrane (AEM, Selemion, Japan) was used to separate the anodic and cathodic chamber. The electrocatalysts were mixed with Nafion binder solution (0.16 wt %) to adhere onto 1 × 1 cm^2 carbon paper (CP) as the working electrode. The catalyst loading was maintained at 1 mg/cm^2 for all materials, unless specified. The cyclic voltammetry (CV) measurement was carried out at a scan rate of 5 mV/s, and linear sweep voltammetry (LSV) was measured with a scan rate of 1 mV/s. The active oxygen equivalent was analyzed by a KI−starch titration method referring to the previous literature with some modifications.[63−65] Briefly, a certain amount of the synthesized nickel peroxide powder is dispersed in a 100 mL solution containing acetic acid (HOAc, 0.1 M), potassium acetate (KOAc, 0.1 M), potassium iodide (0.1 M), and starch (Color indicator), which is preaerated with argon to expel the residual air for interference. The iodide in the solution could be oxidized into I_2 by the highly active oxidative species. It can be observed that the solution will change to dark blue after the addition of the nickel peroxide powder due to the chromogenic response between the formed I_2 and starch. Then, the standard sodium thiosulfate solution is titrated into the mixture until the color disappears. Quantitative results were obtained by the normalized comparison to standard oxidation reaction by oxygen atoms (oxygen equivalent). Nickel peroxides obtained from different treatment periods indicate a series of oxygen equivalent per catalyst to correlate with electrochemical urea oxidation performance.

ASSOCIATED CONTENT

Supporting Information

The Supporting Information is available free of charge at https://pubs.acs.org/doi/10.1021/jacsau.3c00245.

Additional experimental details and calculation details (PDF)

AUTHOR INFORMATION

Corresponding Authors

Ming Gong − *Department of Chemistry and Shanghai Key Laboratory of Molecular Catalysis and Innovative Materials, Fudan University, Shanghai 200438, P. R. China;* orcid.org/0000-0002-1584-1211; Email: gongm@fudan.edu.cn

Xuejing Yang − *School of Mechanical and Power Engineering, East China University of Science and Technology, Shanghai 200237, China;* orcid.org/0000-0001-5144-4400; Email: xj.yang@ecust.edu.cn

Ye-Fei Li − *Department of Chemistry and Shanghai Key Laboratory of Molecular Catalysis and Innovative Materials, Fudan University, Shanghai 200438, P. R. China; Key Laboratory of Computational Physical Science, Fudan University, Shanghai 200438, P. R. China;* orcid.org/0000-0003-4433-7433; Email: yefeil@fudan.edu.cn

https://doi.org/10.1021/jacsau.3c00245
JACS Au 2023, 3, 2964−2972

Authors

Yizhou Yang − *School of Mechanical and Power Engineering, East China University of Science and Technology, Shanghai 200237, China*

Jili Li − *Department of Chemistry and Shanghai Key Laboratory of Molecular Catalysis and Innovative Materials, Fudan University, Shanghai 200438, P. R. China*

Chong Li − *School of Mechanical and Power Engineering, East China University of Science and Technology, Shanghai 200237, China*

Xue Wang − *School of Mechanical and Power Engineering, East China University of Science and Technology, Shanghai 200237, China*

Hualin Wang − *School of Mechanical and Power Engineering, East China University of Science and Technology, Shanghai 200237, China*

Zhi-Pan Liu − *Department of Chemistry and Shanghai Key Laboratory of Molecular Catalysis and Innovative Materials, Fudan University, Shanghai 200438, P. R. China; Key Laboratory of Computational Physical Science, Fudan University, Shanghai 200438, P. R. China;* orcid.org/0000-0002-2906-5217

Complete contact information is available at: https://pubs.acs.org/10.1021/jacsau.3c00245

Author Contributions

[∇]Y.Y. and J.L. contributed equally. The manuscript was written through contributions of all authors. All authors have given approval to the final version of the manuscript.

Notes

The authors declare no competing financial interest.

ACKNOWLEDGMENTS

We thank Jianan Li and Shengshuo Xu for their generous support. This work was financially supported by grants from the National Key Research and Development Program of China (Nos. 2019YFC1906700, 2019YFC1604602, and 2022YFA1503503), the National Natural Science Foundation of China (Nos. 22222602, 22006039, 21876049, 21972023, 21773032, and 22022301), China Postdoctoral Science Foundation (2019M661412), Strategic Priority Research Program of the Chinese Academy of Sciences (XDA23010400), and the Innovation Program from CECEP China (cecep-zdkj-2021-006).

ABBREVIATIONS

SSW, Stochastic Surface Walking; NN, neural network; SOR, selective oxidation reaction; OER, oxygen evolution reaction; XPS, X-ray photoelectron spectroscopy; TGA, thermogravimetric analysis; PES, potential energy surface; MD, molecular dynamics; DFT, density functional theory; ^{b}O, bridging oxide; ^{b}OO, bridging O−O buckle; ^{b}OH, hydroxide component; ^{i}O$_3$, interlayer ozone fragment; GM, global minimum; NP-UV/O$_3$, nickel peroxide synthesis by ultraviolet irradiation and O$_3$; ICP, inductively coupled plasma; UOR, urea oxidation reaction; CV, cyclic voltammetry; ECSA, electrocatalytic active surface area; EIS, electrochemical impedance spectroscopy; EPR, electron paramagnetic resonance

REFERENCES

(1) George, M.; Balachandran, K. Nickel-peroxide oxidation of organic compounds. *Chem. Rev.* **1975**, *75* (4), 491−519.

(2) Boswell, M.; Iler, R. Nickel Catalysts. I. The Effect of the Temperature of Preparation on the Crystal Size and Composition of Nickel Oxide1. *J. Am. Chem. Soc.* **1936**, *58* (6), 924−928.

(3) Nakagawa, K.; Konaka, R.; Nakata, T. Oxidation with nickel peroxide. I. Oxidation of alcohols. *Journal of Organic Chemistry* **1962**, *27* (5), 1597−1601.

(4) Thendral, P.; Shailaja, S.; Ramachandran, M. Nickel peroxide: A more probable intermediate in the Ni (II) catalyzed decomposition of peroxomonosulfate. *International Journal of Chemical Kinetics* **2007**, *39* (6), 320−327.

(5) Terabe, S.; Konaka, R. Electron spin resonance studies on oxidation with nickel peroxide. Spin trapping of free-radical intermediates. *J. Am. Chem. Soc.* **1969**, *91* (20), 5655−5657.

(6) Yoon, H.; Burrows, C. J. Catalysis of alkene oxidation by nickel salen complexes using sodium hypochlorite under phase-transfer conditions. *J. Am. Chem. Soc.* **1988**, *110* (12), 4087−4089.

(7) Konaka, R.; Terabe, S.; Kuruma, K. Mechanism of the oxidation reaction with nickel peroxide. *Journal of Organic Chemistry* **1969**, *34* (5), 1334−1337.

(8) Nakagawa, K.; Tsuji, T. Oxidation with Nickel Peroxide. II. Oxidation of Amines. *Chem. Pharm. Bull.* **1963**, *11* (3), 296−301.

(9) Nakagawa, K.; Onoue, H.; Sugita, J. Oxidation with Nickel Peroxide. IV. The Preparation of Benzoxazoles from Schiff's Bases. *Chem. Pharm. Bull.* **1964**, *12* (10), 1135−1138.

(10) Diaz-Morales, O.; Ferrus-Suspedra, D.; Koper, M. T. M. The importance of nickel oxyhydroxide deprotonation on its activity towards electrochemical water oxidation. *Chem. Sci.* **2016**, *7* (4), 2639−2645.

(11) Martirez, J. M. P.; Carter, E. A. Noninnocent Influence of Host beta-NiOOH Redox Activity on Transition-Metal Dopants' Efficacy as Active Sites in Electrocatalytic Water Oxidation. *ACS Catal.* **2020**, *10* (4), 2720−2734.

(12) Friebel, D.; Louie, M. W.; Bajdich, M.; Sanwald, K. E.; Cai, Y.; Wise, A. M.; Cheng, M. J.; Sokaras, D.; Weng, T. C.; Alonso-Mori, R.; Davis, R. C.; Bargar, J. R.; Norskov, J. K.; Nilsson, A.; Bell, A. T. Identification of Highly Active Fe Sites in (Ni,Fe)OOH for Electrocatalytic Water Splitting. *J. Am. Chem. Soc.* **2015**, *137* (3), 1305−1313.

(13) Bode, H.; Dehmelt, K.; Witte, J. Zur kenntnis der nickel-hydroxidelektrode—I. Über das nickel (II)-hydroxidhydrat. *Electrochim. Acta* **1966**, *11* (8), 1079−1087.

(14) Bender, M. T.; Lam, Y. C.; Hammes-Schiffer, S.; Choi, K. S. Unraveling Two Pathways for Electrochemical Alcohol and Aldehyde Oxidation on NiOOH. *J. Am. Chem. Soc.* **2020**, *142* (51), 21538−21547.

(15) Cairns, R.; Ott, E. X-Ray Studies of the System Nickel—Oxygen—Water. II. Compounds Containing Trivalent Nickel1. *J. Am. Chem. Soc.* **1933**, *55* (2), 534−544.

(16) Moroney, L. M.; Smart, R. S. C.; Roberts, M. W. Studies of the thermal decomposition of β-NiO(OH) and nickel peroxide by X-ray photoelectron spectroscopy. *Journal of the Chemical Society, Faraday Transactions 1: Physical Chemistry in Condensed Phases* **1983**, *79* (8), 1769−1778.

(17) Bond, G. C.; Tripathi, J. B. Investigation of the decomposition and reduction of "nickel peroxide" by thermal analysis. *Journal of the Chemical Society, Faraday Transactions 1: Physical Chemistry in Condensed Phases* **1977**, *73*, 545−552.

(18) Citra, A.; Chertihin, G. V.; Andrews, L.; Neurock, M. Reactions of laser-ablated nickel atoms with dioxygen. Infrared spectra and density functional calculations of nickel oxides NiO, ONiO, Ni2O2, and Ni2O3, superoxide NiOO, peroxide Ni (O2), and higher complexes in solid argon. *J. Phys. Chem. A* **1997**, *101* (17), 3109−3118.

(19) Smith, R. D. L.; Berlinguette, C. P. Accounting for the Dynamic Oxidative Behavior of Nickel Anodes. *J. Am. Chem. Soc.* **2016**, *138* (5), 1561−1567.

(20) Louie, M. W.; Bell, A. T. An Investigation of Thin-Film Ni-Fe Oxide Catalysts for the Electrochemical Evolution of Oxygen. *J. Am. Chem. Soc.* **2013**, *135* (33), 12329−12337.
(21) Gao, M.; Sheng, W.; Zhuang, Z.; Fang, Q.; Gu, S.; Jiang, J.; Yan, Y. Efficient water oxidation using nanostructured α-nickel-hydroxide as an electrocatalyst. *J. Am. Chem. Soc.* **2014**, *136* (19), 7077−7084.
(22) Seh, Z. W.; Kibsgaard, J.; Dickens, C. F.; Chorkendorff, I. B.; Norskov, J. K.; Jaramillo, T. F. Combining theory and experiment in electrocatalysis: Insights into materials design. *Science* **2017**, *355* (6321), eaad4998.
(23) Ma, S. C.; Huang, S. D.; Liu, Z. P. Dynamic coordination of cations and catalytic selectivity on zinc-chromium oxide alloys during syngas conversion. *Nat. Catal* **2019**, *2* (8), 671−677.
(24) Yuan, X. A quantum-computing advantage for chemistry. *Science* **2020**, *369* (6507), 1054−1055.
(25) Zheng, P.; Zubatyuk, R.; Wu, W.; Isayev, O.; Dral, P. O. Artificial Intelligence-Enhanced Quantum Chemical Method with Broad Applicability. *Nat. Commun.* **2021**, 7022.
(26) Martonak, R.; Donadio, D.; Oganov, A. R.; Parrinello, M. Crystal structure transformations in SiO2 from classical and ab initio metadynamics. *Nat. Mater.* **2006**, *5* (8), 623−626.
(27) Amsler, M.; Goedecker, S. Crystal structure prediction using the minima hopping method. *J. Chem. Phys.* **2010**, *133* (22), 224104.
(28) Goedecker, S. Minima hopping: An efficient search method for the global minimum of the potential energy surface of complex molecular systems. *J. Chem. Phys.* **2004**, *120* (21), 9911−9917.
(29) Segler, M. H. S.; Preuss, M.; Waller, M. P. Planning chemical syntheses with deep neural networks and symbolic AI. *Nature* **2018**, *555* (7698), 604.
(30) Nielsen, M. K.; Ahneman, D. T.; Riera, O.; Doyle, A. G. Deoxyfluorination with Sulfonyl Fluorides: Navigating Reaction Space with Machine Learning. *J. Am. Chem. Soc.* **2018**, *140* (15), 5004−5008.
(31) Shang, C.; Zhang, X.-J.; Liu, Z.-P. Stochastic surface walking method for crystal structure and phase transition pathway prediction. *Phys. Chem. Chem. Phys.* **2014**, *16* (33), 17845−17856.
(32) Shang, C.; Liu, Z.-P. Stochastic Surface Walking Method for Structure Prediction and Pathway Searching. *J. Chem. Theory Comput.* **2013**, *9* (3), 1838−1845.
(33) Shang, C.; Zhang, X. J.; Liu, Z. P. Stochastic surface walking method for crystal structure and phase transition pathway prediction. *Phys. Chem. Chem. Phys.* **2014**, *16* (33), 17845−17856.
(34) Huang, S.-D.; Shang, C.; Zhang, X.-J.; Liu, Z.-P. Material discovery by combining stochastic surface walking global optimization with a neural network. *Chem. Sci.* **2017**, *8* (9), 6327−6337.
(35) Huang, S.-D.; Shang, C.; Kang, P.-L.; Liu, Z.-P. Atomic structure of boron resolved using machine learning and global sampling. *Chem. Sci.* **2018**, *9* (46), 8644−8655.
(36) Wales, D. J.; Doye, J. P. K. Global Optimization by Basin-Hopping and the Lowest Energy Structures of Lennard-Jones Clusters Containing up to 110 Atoms. *J. Phys. Chem. A* **1997**, *101* (28), 5111−5116.
(37) Doye, J. P. K.; Wales, D. J. Thermodynamics of Global Optimization. *Phys. Rev. Lett.* **1998**, *80* (7), 1357−1360.
(38) Wales, D. J.; Scheraga, H. A. Global Optimization of Clusters, Crystals, and Biomolecules. *Science* **1999**, *285* (5432), 1368.
(39) Harris, K. D. M.; Habershon, S.; Cheung, E. Y.; Johnston, R. L. Developments in genetic algorithm techniques for structure solution from powder diffraction data%J Zeitschrift für Kristallographie - Crystalline. *Materials.* **2004**, *219* (12), 838−846.
(40) Oganov, A. R.; Glass, C. W. Crystal structure prediction using ab initio evolutionary techniques: Principles and applications. *J. Chem. Phys.* **2006**, *124* (24), 244704.
(41) Li, J.-L.; Li, Y.-F.; Liu, Z.-P. In Situ Structure of a Mo-Doped Pt-Ni Catalyst during Electrochemical Oxygen Reduction Resolved from Machine Learning-Based Grand Canonical Global Optimization. *JACS Au* **2023**, *3* (4), 1162−1175.
(42) Lin, C.; Li, J.-L.; Li, X.; Yang, S.; Luo, W.; Zhang, Y.; Kim, S.-H.; Kim, D.-H.; Shinde, S. S.; Li, Y.-F.; Liu, Z.-P.; Jiang, Z.; Lee, J.-H. In-situ reconstructed Ru atom array on α-MnO2 with enhanced performance for acidic water oxidation. *Nature Catalysis* **2021**, *4* (12), 1012−1023.
(43) Ma, S.; Huang, S.-D.; Liu, Z.-P. Dynamic coordination of cations and catalytic selectivity on zinc-chromium oxide alloys during syngas conversion. *Nature Catalysis* **2019**, *2* (8), 671−677.
(44) Huang, S.-D.; Shang, C.; Kang, P.-L.; Zhang, X.-J.; Liu, Z.-P. LASP: Fast global potential energy surface exploration. *Wiley Interdisciplinary Reviews-Computational Molecular Science* **2019**, *9* (6), e1415.
(45) Bachmann, J.; Zolotaryov, A.; Albrecht, O.; Goetze, S.; Berger, A.; Hesse, D.; Novikov, D.; Nielsch, K. Stoichiometry of Nickel Oxide Films Prepared by ALD. *Chem. Vap. Deposition* **2011**, *17* (7−9), 177−180.
(46) Neubecker, A.; Pompl, T.; Doll, T.; Hansch, W.; Eisele, I. Ozone-enhanced molecular beam deposition of nickel oxide (NiO) for sensor applications. *Thin Solid Films* **1997**, *310* (1), 19−23.
(47) Anisimov, V. I.; Zaanen, J.; Andersen, O. K. Band theory and Mott insulators: Hubbard U instead of Stoner I. *Phys. Rev. B* **1991**, *44* (3), 943−954.
(48) Li, Y.-F.; Selloni, A. Mechanism and Activity of Water Oxidation on Selected Surfaces of Pure and Fe-Doped NiOx. *ACS Catal.* **2014**, *4* (4), 1148−1153.
(49) Hall, D. S.; Lockwood, D. J.; Bock, C.; MacDougall, B. R. Nickel hydroxides and related materials: a review of their structures, synthesis and properties. *Proceedings of the Royal Society A: Mathematical, Physical and Engineering Sciences* **2015**, *471* (2174), 20140792.
(50) Qiu, Z.; Ma, Y.; Edvinsson, T. In operando Raman investigation of Fe doping influence on catalytic NiO intermediates for enhanced overall water splitting. *Nano Energy* **2019**, *66*, 104118.
(51) Islam, R.; Chen, G.; Ramesh, P.; Suh, J.; Fuchigami, N.; Lee, D.; Littau, K. A.; Weiner, K.; Collins, R. T.; Saraswat, K. C. Investigation of the Changes in Electronic Properties of Nickel Oxide (NiOx) Due to UV/Ozone Treatment. *ACS Appl. Mater. Interfaces* **2017**, *9* (20), 17201−17207.
(52) Dupin, J.-C.; Gonbeau, D.; Vinatier, P.; Levasseur, A. Systematic XPS studies of metal oxides, hydroxides and peroxides. *Phys. Chem. Chem. Phys.* **2000**, *2* (6), 1319−1324.
(53) Soler, L.; Casanovas, A.; Escudero, C.; Pérez-Dieste, V.; Aneggi, E.; Trovarelli, A.; Llorca, J. Ambient Pressure Photoemission Spectroscopy Reveals the Mechanism of Carbon Soot Oxidation in Ceria-Based Catalysts. *ChemCatChem.* **2016**, *8* (17), 2748−2751.
(54) Au, C. K. Coulomb-gauge electrodynamics analysis of two-photon exchange in electron-atom scattering. II. Interaction at all distances beyond atomic dimensions. *Phys. Rev. A* **1988**, *38* (1), 7−12.
(55) Idriss, H. On the wrong assignment of the XPS O1s signal at 531−532 eV attributed to oxygen vacancies in photo- and electro-catalysts for water splitting and other materials applications. *Surf. Sci.* **2021**, *712*, 121894.
(56) Wang, H.; Yong, D. Y.; Chen, S. C.; Jiang, S. L.; Zhang, X. D.; Shao, W.; Zhang, Q.; Yan, W. S.; Pan, B. C.; Xie, Y. Oxygen-Vacancy-Mediated Exciton Dissociation in BiOBr for Boosting Charge-Carrier-Involved Molecular Oxygen Activation. *J. Am. Chem. Soc.* **2018**, *140* (5), 1760−1766.
(57) Stoyanova, R.; Zhecheva, E.; Alcantara, R.; Tirado, J. L. Local Coordination of Low-Spin Ni3+ Probes in Trigonal LiAlyCo1-yO2 Monitored by HF-EPR. *The Journal of Physical Chemistry B* **2004**, *108* (13), 4053−4057.
(58) Polliotto, V.; Livraghi, S.; Agnoli, S.; Granozzi, G.; Giamello, E. Reversible adsorption of oxygen as superoxide ion on cerium doped zirconium titanate. *Applied Catalysis A: General* **2019**, *580*, 140−148.
(59) Manigrasso, J.; Chillón, I.; Genna, V.; Vidossich, P.; Somarowthu, S.; Pyle, A. M.; De Vivo, M.; Marcia, M. Author Correction: Visualizing group II intron dynamics between the first and second steps of splicing. *Nat. Commun.* **2022**, *13* (1), 1.

https://doi.org/10.1021/jacsau.3c00245
JACS Au 2023, 3, 2964−2972

(60) Kuai, C.; Xu, Z.; Xi, C.; Hu, A.; Yang, Z.; Zhang, Y.; Sun, C.-J.; Li, L.; Sokaras, D.; Dong, C.; Qiao, S.-Z.; Du, X.-W.; Lin, F. Phase segregation reversibility in mixed-metal hydroxide water oxidation catalysts. *Nature Catalysis* **2020**, *3* (9), 743−753.
(61) Corrigan, D. A.; Knight, S. L. Electrochemical and spectroscopic evidence on the participation of quadrivalent nickel in the nickel hydroxide redox reaction. *J. Electrochem. Soc.* **1989**, *136* (3), 613.
(62) Li, J.; Li, J.; Liu, T.; Chen, L.; Li, Y.; Wang, H.; Chen, X.; Gong, M.; Liu, Z.-P.; Yang, X. Deciphering and Suppressing Over-Oxidized Nitrogen in Nickel-Catalyzed Urea Electrolysis. *Angew. Chem., Int. Ed.* **2021**, *60* (51), 26656−26662.
(63) Skellon, J.; Wills, E. Iodimetric methods of estimating peroxidic oxygen. *Analyst* **1948**, *73* (863), 78−86.
(64) Cairns, R.; Ott, E. X-Ray Studies of the System Nickel—Oxygen—Water. II. Compounds Containing Trivalent Nickel1. *J. Am. Chem. Soc.* **1933**, *55* (2), 534−544.
(65) Corrigan, D. A.; Knight, S. L. Electrochemical and spectroscopic evidence on the participation of quadrivalent nickel in the nickel hydroxide redox reaction. *J. Electrochem. Soc.* **1989**, *136* (3), 613.

https://doi.org/10.1021/jacsau.3c00245
JACS Au 2023, 3, 2964−2972